Imaging continental breakup using teleseismic body waves: The Woodlark Rift, Papua New Guinea

Zachary Eilon[1], Geoffrey A Abers[2,3], James B Gaherty[3], and Ge Jin[1]

[1]Department of Earth and Environmental Sciences, Lamont-Doherty Earth Observatory of Columbia University, Palisades, New York, USA, [2]Department of Earth and Atmospheric Science, Cornell University, Ithaca, New York, USA, [3]Lamont-Doherty Earth Observatory of Columbia University, Palisades, New York, USA

Key Points:
- Body wave inversion for mantle structure within highly extended continental rift
- Slow, narrow rift axis demonstrates mantle extension ahead of seafloor breakup
- Well-constrained thermal contrast between rift and fast seismogenic structure

Supporting Information:
- Supporting Information S1
- Supporting Information S2
- Figure S1
- Figure S2
- Figure S3
- Table S1

Correspondence to:
Z. Eilon,
zeilon@ldeo.columbia.edu

Abstract This study images the upper mantle beneath the D'Entrecasteax Islands, Papua New Guinea, providing insight into mantle deformation beneath a highly rifted continent adjacent to propagating spreading centers. Differential travel times from *P* and *S*-wave teleseisms recorded during the 2010–2011 CDPapua passive seismic experiment are used to invert for separate V_P and V_S velocity models of the continental rift. A low-velocity structure marks the E-W axis of the rift, correlating with the thinnest crust, high heat flow, and a linear trend of volcanoes. This slow region extends 250 km along strike from the oceanic spreading centers, demonstrating significant mantle extension ahead of seafloor breakup. The rift remains narrow to depth indicating localization of extension, perhaps as a result of mantle hydration. A high-V_P structure at depths of 90–120 km beneath the north of the array is more than 6.5% faster than the rift axis and contains well-located intermediate depth earthquakes. These independent observations place firm constraints on the lateral thermal contrast at depth between the rift axis and cold lithosphere to the north that may be related to recent subduction, although the polarity of subduction cannot be resolved. This geometry is gravitationally unstable; downwelling or small-scale convection could have facilitated rifting and rapid lithospheric removal, although this may require a wet mantle to be realistic on the required time scales. The high-*V* structure agrees with the maximum P,T conditions recorded by young ultra-high pressure rocks exposed on the rift axis and may be implicated in their genesis.

1. Introduction

1.1. Overview

The Woodlark Rift, in southeastern Papua New Guinea, is one of the youngest and most rapidly extending continental rifts in the world. It hosts the youngest known ultra-high pressure (UHP) rocks, exhuming at ∼20 mm/yr by a mechanism that remains unclear [*Baldwin et al.*, 2008; *Gordon et al.*, 2012; *Webb et al.*, 2008; *Ellis et al.*, 2011; *Little et al.*, 2011]. This region is one of the few active examples of a mid-ocean ridge tip propagating into thinning continental crust, spanning the transition from lithospheric extension to seafloor spreading (Figure 1).

The CDPapua experiment images the mantle of this continental rift in detail. Body wave tomography reveals the mantle structure of the rifted continent just west of the spreading center. From these images, we address the following questions: How does the mantle behave during continental rifting? Is seismologically observed structure explicable by temperature variation alone, or are additional mechanisms (e.g., melt, lithology, volatiles) required? Can we image structures that are candidate sources for UHP rocks? Is there a relationship between this region's history of recent subduction and the present rifting?

1.2. Tectonic Setting

Since the late Miocene, the Woodlark and Solomon Sea (SOL) microplates have been rotating northward relative to Australia (AUS), about a nearby Euler pole to their west [*Taylor et al.*, 1999; *Wallace et al.*, 2004, 2014]. The resultant north-south-opening basin evinces maximal extension in the east, where seafloor spreading developed ∼6 Ma, and grades toward minimally thinned continental crust in the west. With time, the spreading centers have propagated westward into the continent. Magnetic lineations in the young seafloor to the East imply up to 140–190 km of extension at the longitude of the D'Entrecasteaux Islands (DEI) [*Taylor et al.*, 1999]. While others have challenged these estimates as incompatible with surficial expressions of extension [*Kington and Goodliffe*, 2008], in the absence of an obvious transfer structure it is not clear how else to accommodate the far-field motions. GPS data, reflection seismology, and geologic observations
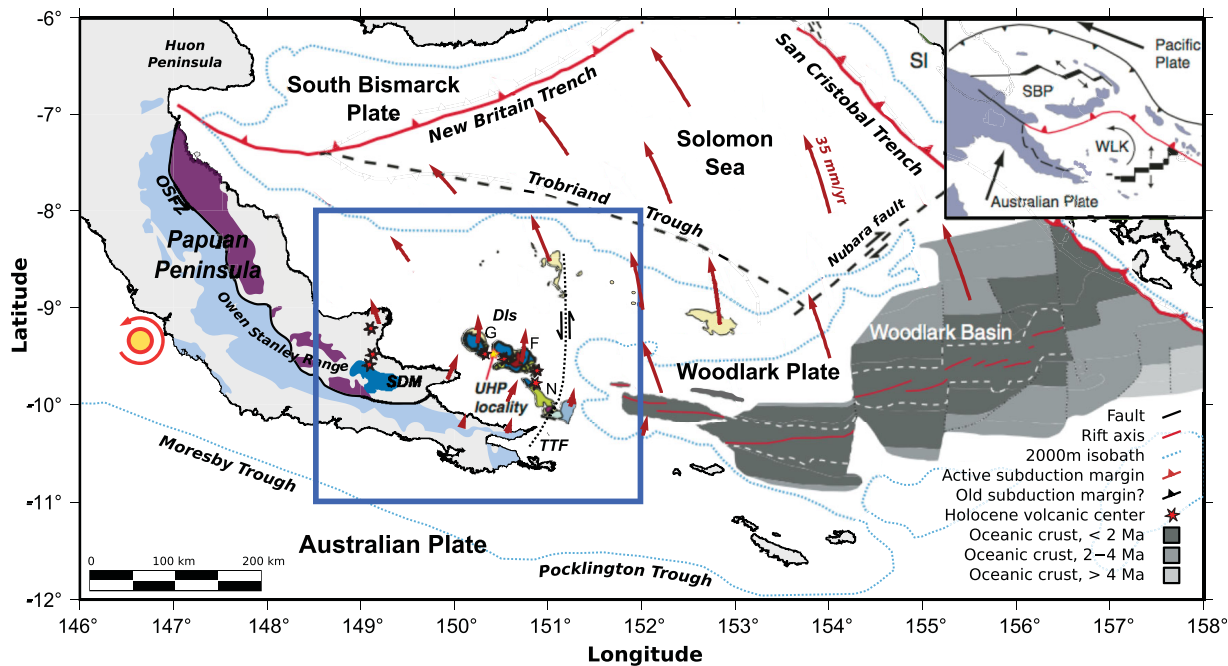
Figure 1. Tectonic map of southeastern Papua New Guinea, modified after *Baldwin et al*. [2008]. Red arrows: present-day plate motions with respect to Australia (AUS) according to best fitting GPS model [*Wallace et al.*, 2014]. Yellow circle: Euler pole for 4.02°/Myr rotation of the Woodlark Plate (WLK) with respect to AUS from 3.6 to 0.5 Ma [*Taylor et al.*, 1999]. Oceanic crust shown by gray shading, Brunes chron indicated by white dashed line, and recent shift in tectonics evident from the obliquity of present spreading ridges to magnetic isochrons. Purple shaded: Papuan Ultramafic Belt; light blue shaded: Owen-Stanley Metamorphics. DIs: D'Entrecasteaux Islands; TTF: Trobriand Transfer Fault, shown with geologic left-lateral slip although recent GPS results indicate right-lateral motion [*Wallace et al.*, 2014]; OSFZ: Owen Stanley Fault Zone. Blue box shows area of field deployment and later figures, Holocene volcanic centers in this region only are depicted. Inset: simplified regional tectonics showing role of WLK and South Bismarck Plate in mobile belt between obliquely converging Australian and Pacific plates.

[*Wallace et al.*, 2014; *Fitz and Mann*, 2013; *Kington and Goodliffe*, 2008] reveal that extension is distributed at the surface across a number of structures, including strain within Goodenough Basin and possibly on faults bounding the DEI.

Quaternary volcanism along an east-west line of volcanoes extends approximately along strike from the youngest seafloor spreading centers. These volcanoes produce calc-alkaline lavas with *K* and *Ba/La* signatures indicative of a subduction-enriched source [*Smith and Milsom*, 1984] although no proximate subduction is presently evident, and no slab has previously been identified from seismicity or regional tomography. During the Cenozoic, the Papuan orogenic belt developed on the mainland and along the Papuan Peninsula as ophiolites, arcs, and subduction complexes accreted to the leading edge of the Australian plate on north dipping thrust faults [*Davies and Jaques*, 1984]. Scattered intermediate depth seismicity extending from the northern coastal ranges (146°E) southeastward beneath the Papuan Peninsula near 100–150 km depth is related to subduction [*Pegler et al.*, 1995] or lithospheric instability [*Abers and Roecker*, 1991].

The DEI are cored by high pressure metamorphic rocks at the surface, including a UHP coesite-eclogite that records conditions of ∼3 GPa as recently as 5–8 Ma [*Baldwin et al.*, 2004; *Gordon et al.*, 2012]. Physical mechanisms suggested for accommodating uplift at ∼20 mm/yr include low-angle detachment zones [*Webb et al.*, 2008], eduction (K. D. Petersen, and W. R. Buck, Eduction, extension and exhumation of ultra-high pressure rocks in metamorphic core complexes due to subduction initiation, submitted to *Geochemistry Geophysics Geosystems*, doi:10.1002/2015GC005847, 2015) and diapirism [*Ellis et al.*, 2011; *Little et al.*, 2011]. *Abers et al*. [1997] found that shallowly dipping faults bounding the easternmost domes are actively accommodating exhumation via low-angle normal faulting earthquakes, synchronous with extension.

2. Data

2.1. Deployment and Measurement of Travel Times

The CDPapua passive seismic experiment comprised 31 on-land broadband PASSCAL stations, as well as 8 broadband OBS, deployed for ∼15 months between March 2010 and July 2011 (Figure 2 and supporting
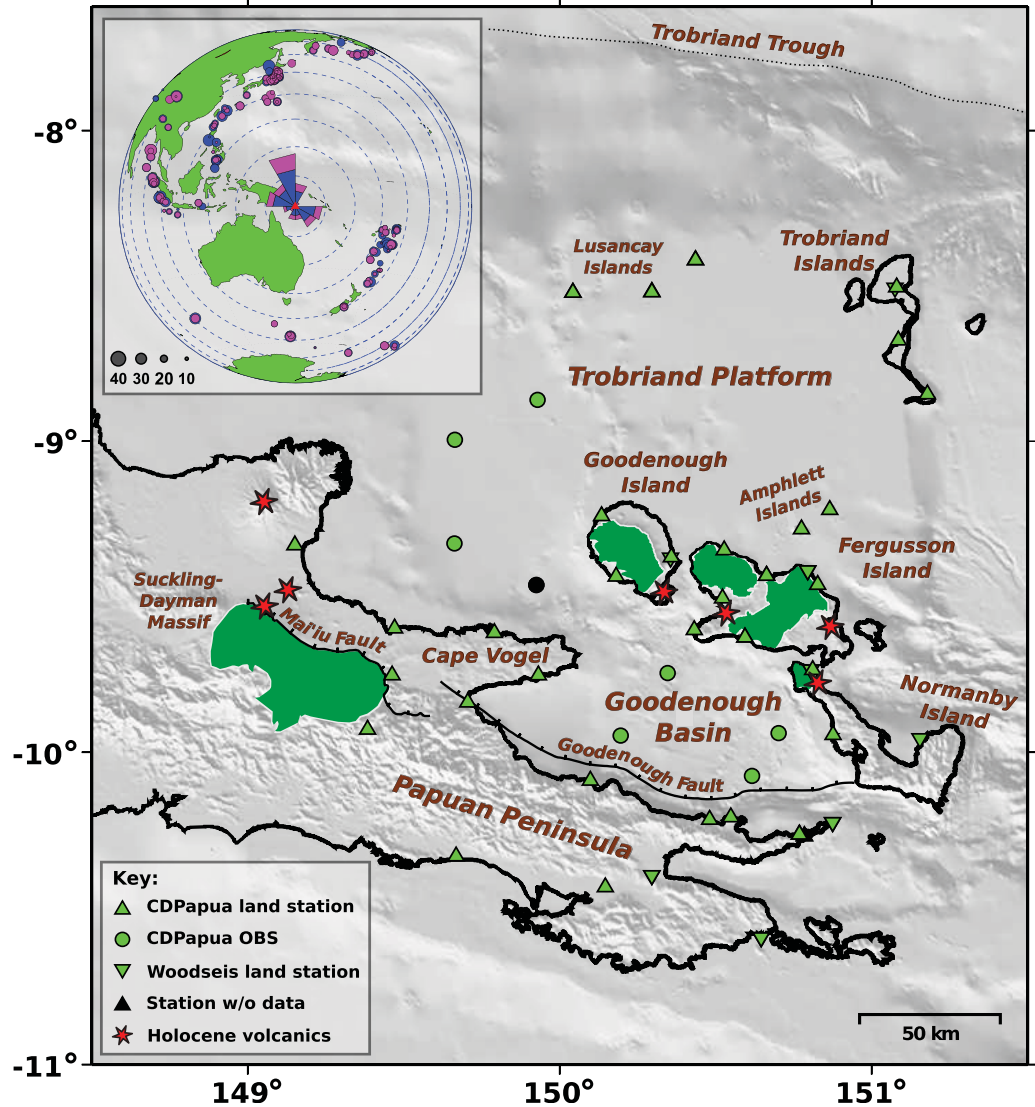
Figure 2. Map showing the geography of the region, with station locations, including those from the 2000–2001 Woodseis experiment. Inset: Distribution of teleseismic earthquakes used for *P* (blue) and *S* (magenta) tomography, where symbol size indicates number of cross-correlated arrivals and contours are 10° increments from the array center (red triangle). The rose-diagram describing back-azimuthal distribution is area-proportional.

information Table S1). The aperture of the array was approximately 250 km with station spacing of 20–50 km, suitable for teleseismic tomography between 50 and 250 km depth.

We measured body wave arrivals from 218 teleseismic earthquakes between 5 March 2010 and 30 July 2011. This data set included 3554 direct *P* arrivals from 192 events and 2810 direct *S* arrivals from 172 events in a distance range of 30–90° from the center of our array (with the exception of four events >90° away that had strong diffracted phases). 91 *PKP* travel times for six selected events were also used; these near-vertically incident rays improve the lateral resolution of our model. A data set of >600 teleseismic *P* arrivals from 90 events measured on the 1999–2000 Woodseis array [*Abers et al.*, 2002] supplement our data, extending the region of coverage further to the east.

We use a modern implementation of the ACH tomography approach [*Aki et al.*, 1977], accounting for expected move-out across the array to measure differential travel times of *P* and *S* phases. This approach relies on the assumption that moveout-corrected travel time variations are due to velocity heterogeneities within our model volume, while an event time residual captures integrated effects of velocity variations outside our model volume.
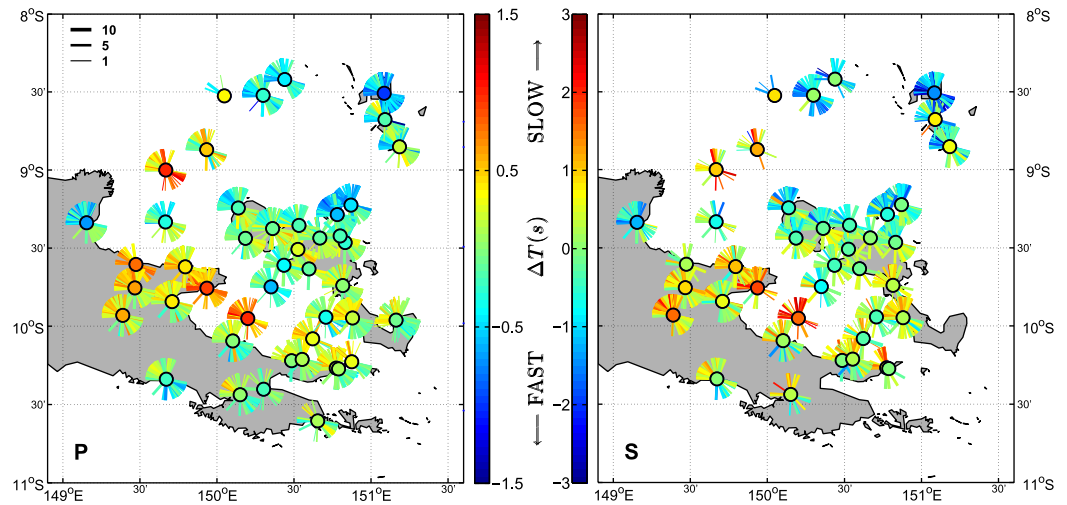
Figure 3. Differential travel times (lines) for teleseismic (left) *P* waves and (right) *S* waves, plotted by incoming azimuth. The colored line thicknesses are scaled to the data weighting (see legend, top-left). Circles at station locations indicate crustal terms solved for in the inversion (section 4.1 and supporting information Table S1), exaggerated by 2×.

Each set of body wave arrivals was filtered and windowed by eye to preserve as much high frequency information as possible, including just the first couple of oscillations. The mean center frequency used for the *P* waves was 0.5 Hz and for *S* waves was 0.12 Hz; the precise center frequency used for each set of arrivals was later used to calculate finite-frequency kernels. Multichannel cross correlation [*VanDecar and Crosson*, 1990] of the filtered, windowed traces was performed to obtain arrival times relative to predictions calculated with TauP (using velocity model IASP91) [*Crotwell et al.*, 1999].

Eilon et al. [2014a] established that this region contains strong anisotropy with N-S fast geometry within the rift. Recent work [*Eilon et al.*, 2014b] indicates heterogeneous anisotropy throughout this region; the degree to which this influences *S* wave first-arrival times will depend on polarization and is not straightforward to remove. We separately measured *S* relative delay times on BHN and BHE channels and for this isotropic inversion used delay times of *S* waves on whichever component had more arrivals or higher mean values of cross correlation maxima—the preferred component is generally related to the *S*-wave polarization. This procedure prioritises the highest quality travel time measurements, while the "noise" introduced by anisotropy will be averaged out over multiple events and will contribute to inversion misfit; alternative approaches, such as using the transverse component, would have similar distortion due to anisotropy but in general lower signal-to-noise level.

In total, the data set comprised 4257 *P* arrivals and 2810 *S* arrivals with RMS differential travel times of 0.396 s and 0.983 s respectively. The earthquakes were well distributed with respect to azimuth and distance around our region of interest (Figure 2), although there was a relative paucity of arrivals from the NE and SW octants and disproportionate illumination from the north due to aftershocks of the great Tohoku earthquake in March 2011.

Following *Schmandt and Humphreys* [2010a] we describe the spatial coverage of the data by the "hit quality" parameter, a combined measure of the hit count and the back-azimuthal coverage for each voxel. This function is calculated as the number of rays with sensitivity in each voxel from each back-azimuthal hexant, with the count saturating at a maximum of 6 rays per hexant, giving a total score out of 36 that is normalized to a value between 0 and 1. Within the array our spatial coverage is excellent, indicating that models should be able to faithfully resolve lateral heterogeneities. Outside the array, and at greater depth, hit quality deteriorates.

2.2. Travel Time Residuals

Both *P* and *S* differential travel time maps (Figure 3) show an E-W swath of positive delay times beneath the center of the array, indicating that a relatively slow region of upper mantle underlies the DEI, Goodenough Basin, and Cape Vogel, compared to faster structure to the north and south.

This data set also reveals marked back azimuthal variation of delay time at several stations, for example, on the NW coast of Goodenough Island, or on the northern coast of the Papuan Peninsula at 150.8°E. Such strong variation is an indicator of lateral velocity gradients directly beneath the station. While anisotropy is strong in this region, isotropic velocity heterogeneities better explain the spatial pattern of the sites with strong back-azimuthal variation.

In the far north of the array several stations have large travel time deficits, implying fast structure. By contrast, several of the OBS stations (particularly to the NW of Goodenough Island, and in the SW of Goodenough Basin) have marked travel time delays compared to stations close to them. These stations lie on some of the thickest sediments in this region (between 3.0 and 5.0 s two-way travel time to basement) [*Fitz and Mann*, 2013] and have large station static terms in the inversion.

3. Tomographic Method

3.1. Finite Frequency Kernels

We apply a finite frequency approach to inverting for seismic velocities, following the approach of *Schmandt and Humphreys* [2010a] who use a first Fresnel zone paraxial approximation to the Born theoretical kernel [*Dahlen et al.*, 2000], based on 1-D ray tracing in the AK135 reference model [*Kennett et al.*, 1995]. These simplified kernels are advantageous in terms of computational efficiency, and are suitable given imprecise knowledge of the true ray path in a 3-D heterogeneous Earth.

The kernel is calculated by finding the ray-normal first Fresnel zone radius, R_f at 15 km increments along the ray, as a function of velocity (v), distance along the ray (D_R), frequency (f), and total path length (Δ):

$$R_f = \sqrt{\left(\frac{v}{f}\right)\frac{D_R(\Delta - D_R)}{\Delta}} \tag{1}$$

These radii are interpolated along the ray path and then used to compute a ray-normal sensitivity function that approximates the bimodal Born kernel, without side-lobes [*Schmandt and Humphreys*, 2010a, equation (2)]. The kernel is normalized to the ray theoretical sensitivity along the path [*Schmandt and Humphreys*, 2010a, equation (3)] such that for velocity heterogeneities wider than the sensitivity kernel the predicted travel time anomaly using the finite frequency approach is identical to the ray theoretical prediction. Finally, ray-normal smoothing is applied (calibrated by the results of *Saltzer and Humphreys* [1997]), where smoothing increases with distance from the station.

3.2. Parameterization and Regularization

Differential velocities are computed on an irregular rectangular mesh of nodes. The node spacing increases with distance from the center of the array, from 30 (within the array) to 45 km, and increases with depth from 30 km in the shallowest mantle to 40 km at the base of the model domain, at 290 km.

We apply both spatial smoothing and model norm damping to regularize the inverse problem, which then minimizes the cost function:

$$E = ||\omega(\mathbf{Gm} - \mathbf{d}_{obs})||^2 + \gamma||\mathbf{Lm}||^2 + \epsilon||\mathbf{m}||^2 \tag{2}$$

where **m** is the vector of perturbations to the initial velocity model, $\mathbf{d}_{obs}$ is the vector of differential travel times, and **G** is the matrix with $G_{ij} = \partial d_i / \partial m_j$. ω is a diagonal matrix of data weights, γ is the smoothing parameter, **L** is a smoothing matrix that applies an exponentially decaying covariance between nearby grid points [*Menke and Eilon*, 2015], and ϵ is the damping parameter.

We analyze the trade-off between model roughness and data misfit (supporting information Figure S1) to determine regularization parameters where model roughness and data misfit are mutually minimized [*Menke*, 1984]. γ and ϵ are given by the minimum of the penalty function, $\chi = ||\mathbf{Gm} - \mathbf{d}_{obs}||^2 + 2||\mathbf{m}||^2$, where our choice to penalize model roughness by twice as much as data misfit is arbitrary and selected to give a model with the most realistic structure. For close-to-optimal values of damping (ϵ between ∼1 and ∼10) the strength of smoothing (γ) does not have a large effect on the penalty function (supporting information Figure S1) demonstrating that ϵ has more influence over the location of the L-curve

corner. We favor slight over-damping to yield only the most robust features, which are not dependent on nodal geometry.

The model parameter vector, **m** consists of a vector of velocity perturbations at each node in the model (of which there are $n_x \times n_y \times n_z$), as well as n_{sta} static station terms and n_{evt} static event terms. The static terms are intended to account for travel time residuals caused by local site effects and velocity heterogeneities outside of the model volume. *P* and *S* models are determined separately. Large static terms decrease effective time delays that must be accounted for within the model volume and thus mute model structure. In order to avoid these static corrections spuriously removing velocity heterogeneity from the model, we apply limited damping to these station and event terms equal to 50% and 10% of the velocity damping values, respectively.

A series of tests allows us to ascertain the influence of an *a priori* crustal correction versus station static terms solved for in the inversion. The prior crustal terms are computed using a Moho surface from receiver functions and a surface wave V_S model (G. Jin et al., Shear-velocity structure of the D'Entrecasteaux Islands, Papua New Guinea from Rayleigh-wave tomography, submitted to *Geochemistry Geophysics Geosystems*, 2015) with mean V_P/V_S of *Ferris et al.* [2006]. The data are inverted with and without any prior crustal correction, and for the cases of high, moderate, and zero station static damping. These cases correspond to permitting zero, moderate, and unconstrained variation to prior crustal corrections, respectively. Without station static terms the variance reduction for both *P* and *S* models is diminished by ∼10%.

The most important result was that the overall structure of the rift below 50 km (where the rays begin to cross) is unaffected by the prior crustal model used; models vary by an average of just 2.5% between cases employing a prior crustal correction and those without. Changing crustal model affects only the uppermost (40 km) layer in the model and we therefore do not interpret this layer. The station static terms in the inversion absorb the effect of the crust, giving a similar final result whether or not a prior crustal model is imposed.

3.3. Solving the Inverse Problem

The linear inverse problem is solved by applying the LSQR algorithm [*Paige and Saunders*, 1982] to the weighted, damped least squares problem by minimizing *E* in Equation 2. The data weights are based on the maximum value of the maximum cross correlation (C_i) between each trace and the stack for that event, where $\omega_i = 10^{(C_i - 0.7)/0.3}$. The 1-D ray tracing used to compute travel time kernels ignores focusing/defocusing caused by 3-D velocity heterogeneity, with the result that fast features will tend to be artificially broadened, slow features to be artificially thinned, and side lobes to appear [*Bijwaard and Spakman*, 2000]. However, given the coarse grid spacing of >30 km and the small model volume this factor is not likely to introduce large spurious structure into our models. Some of these problems are also obviated by the use of finite-frequency kernels, which are only computed for 1-D reference structures [*Dahlen et al.*, 2000]. The goodness of fit to our data is quantified by the variance reduction:

$$\Delta \text{Var} = \left(1 - \frac{\text{Var}(\mathbf{d}_{obs} - \mathbf{d}_{pred})}{\text{Var}(\mathbf{d}_{obs})} \right) \tag{3}$$

where Var is the variance function, normalized by $n-1$, $\mathbf{d}_{obs}$ is the observed data and $\mathbf{d}_{pred}$ is the data predicted from the model, i.e., $\mathbf{d}_{pred} = \mathbf{Gm}$. This measure of the variance reduction is somewhat inflated as it includes data from poorly resolved regions that are underdetermined and hence bound to be well-fit. Following *Schmandt and Humphreys* [2010b] we also compute the variance reduction (ΔVar_{hq}) using data predicted only from the part of the model domain that is well resolved (section 4.1).

3.4. Synthetic Tests

A suite of synthetic tests demonstrates the ability of these data to usefully resolve structure. Checkerboard tests (Figure 4) demonstrate that our data can accurately recover structure on the order of 90 km in the upper 150 km of both V_P and V_S models. These tests indicate that vertical resolution remains adequate down to ∼150km depth for V_P and ∼100 km depth for V_S. Northward smearing evident deeper than 150 km is likely the result of a preponderance of arrivals from this azimuth (Figure 2).

Our models have an maximum amplitude recovery of ∼80% (*P*) and ∼75% (*S*) in the shallower 150 km of the domain, deteriorating to ∼60% (*P*) and ∼50% (*S*) in the lower 150 km. Following *Zelt* [1998] we compute

Figure 4. Results of checkerboard tests. Left column: input structure; center column: *P* model output structure; right column: *S* model output structure. Top three rows: horizontal tomograms at different depths; bottom row: a north-south vertical section at 148.8°E. The output models are contoured by model semblance (a measure of agreement between the input and output checkerboards) following *Zelt* [1998].

the semblance between the input and output checkerboard models (contours in Figure 4). Values of semblance greater than 0.7 indicate good model fidelity.

Checkerboard tests suffer from the weakness that they simultaneously accentuate smearing along diagonals and underestimate smearing along cardinal directions; as such, they do a poor job of identifying artifacts in the output of the inversion. We performed tests inverting artificial data from a model comprising structures of interest: an E-W slow "ridge axis" and a deeper fast structure in the north of the model (supporting information Figure S2).

These tests demonstrate that the data can resolve V_P structure of a narrow rift, with little horizontal smearing in the upper 150 km. Vertical smearing increases with depth from <50 km in the upper 150 km of the model to ~100 km in the lower half of the model, with along-ray smearing becoming particularly problematic deeper than 160 km. The V_S inversion gives much the same result, with somewhat greater vertical smearing and poorer amplitude recovery.

Since the velocity perturbations within each layer average to zero, these inversions may lead to artificial side lobes adjacent to velocity anomalies. Synthetics indicate these artifacts are likely to be low amplitude (supporting information Figure S2). However, apparent vertical velocity gradients may arise from our lack of constraints on absolute velocity [cf. *Lévêque and Masson*, 1999].

3.5. Squeezing Tests

The steep incidence angle of teleseisms results in poorer vertical resolution than horizontal resolution. A squeezing test is used to ascertain the minimum depth extent of anomalies required by the data, as follows:

In step (i), we solve

$$\mathbf{G}' \mathbf{m}_1 = \mathbf{d} \tag{4}$$

using the constrained least squares inversion. G' includes strong damping that permits velocity perturbations, $\mathbf{m}_1$, only in the upper part of the model, above the "squeezing depth" (z_{sq}). The residual from this inversion,

$$\mathbf{r} = \mathbf{d} - \mathbf{G}' \mathbf{m}_1 \tag{5}$$

then becomes the data for step (ii), solving this time for the whole model space:

$$\mathbf{G} \mathbf{m}_2 = \mathbf{r} \tag{6}$$

By linearity,

$$\mathbf{m} = \mathbf{m}_1 + \mathbf{m}_2 \tag{7}$$

In this way we obtain a model, $\mathbf{m}$, that is not minimum length but fits as much of the data as possible with structure above the squeezing depth. If none of the data require deep structure, then the residual from step (i) will be small, $\mathbf{m}_2$ will be small, and the final model will have very little structure below the squeezing depth and the same variance reduction as the constrained inversion.

We perform squeezing tests for the V_P model with z_{sq} of varying from 120 to 250 km, quantifying the test results by the fraction of the final ΔVar that is achieved in step (i) and the norm of $\mathbf{m}_2$. For values of z_{sq} > 180 km, $\mathbf{m}_1$ produces >95% of the final variance reduction and $||\mathbf{m}_2||_2$ is 85% reduced, i.e., the great majority of the signal can be fit with structure shallower than 180 km and only weak features are required below this depth. This finding does not preclude still deeper structure but any deeper features are not necessitated by our measured time delays. A similar set of tests for the V_S model also shows that features deeper than 180 km are also not required by those data. For $z_{sq} \leq 150$ km the appearance of low velocities along the rift in $\mathbf{m}_2$ indicate that the deep extension of low velocity features in our model is a robust feature.

4. Results

4.1. Tomographic Models

Based on the results of L-curve tests (section 3.2) and the squeezing tests (section 3.5) our preferred P and S models use $\gamma_P = 2$, $\epsilon_P = 5$ and $\gamma_S = 4$, $\epsilon_S = 6$, respectively. The model uncertainty is estimated by bootstrapping using 100 resampled data sets randomly drawn from the full data set. In regions deeper than 50 km with
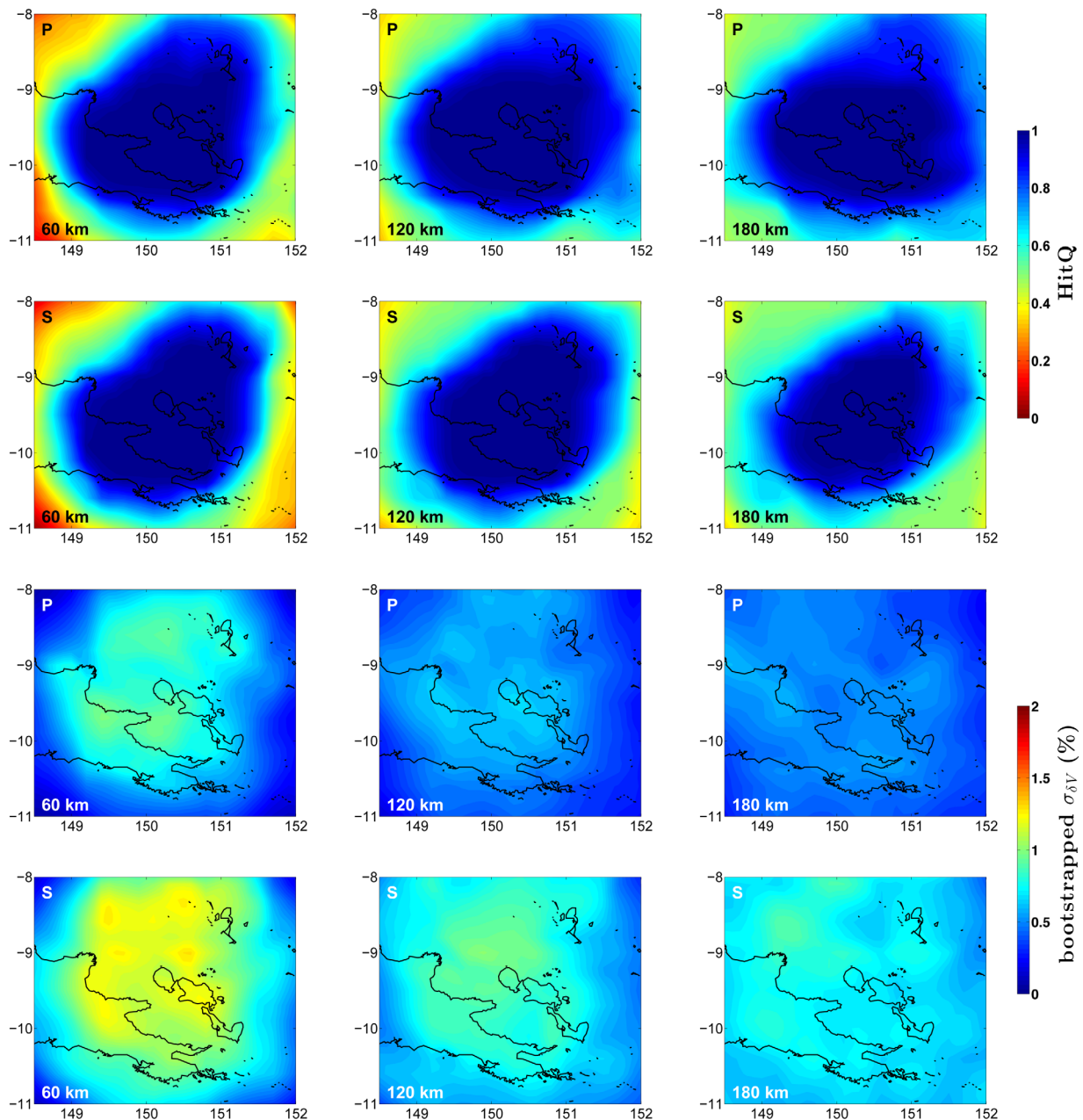
Figure 5. Different measures of model resolution at selected depths. Top pair of rows: hit quality (section 2.1) for (top) *P* and (bottom) *S*. Bottom pair of rows: bootstrapped estimate of standard deviation (section 4.1) of percentage *δV* for (top) *P* and (bottom) *S* models.

hit-quality greater than 0.8 the bootstrapped average standard deviation is 0.53% for δV_P and 0.9% for δV_S. This analysis demonstrates that the main features of the model are well resolved deeper than 50 km. We also note that the region of high checkerboard semblance (> 0.7) closely coincides with the region of high hit-quality and low bootstrapped standard deviation (Figure 5); the fact that these three measures of expected model resolution agree, and that the well resolved region contains much of the interesting structure that we observe, permits us to confidently interpret the images. The consistency of the *P* and *S* models (which are derived from independent data sets) is evident from comparison of Figures 6 and 7 and the robust linear trend in $\delta \ln V_S / \delta \ln V_P$.

The V_P model achieves $\Delta \text{Var} = 82.3\%$ and $\Delta \text{Var}_{hq} = 79.0\%$, while the V_S model, with fewer data and stronger regularization, achieves $\Delta \text{Var} = 76.4\%$ and $\Delta \text{Var}_{hq} = 71.3\%$. Given that the V_P model has 50% more data, with slightly greater spatial coverage, higher frequency information and superior variance reduction, we focus
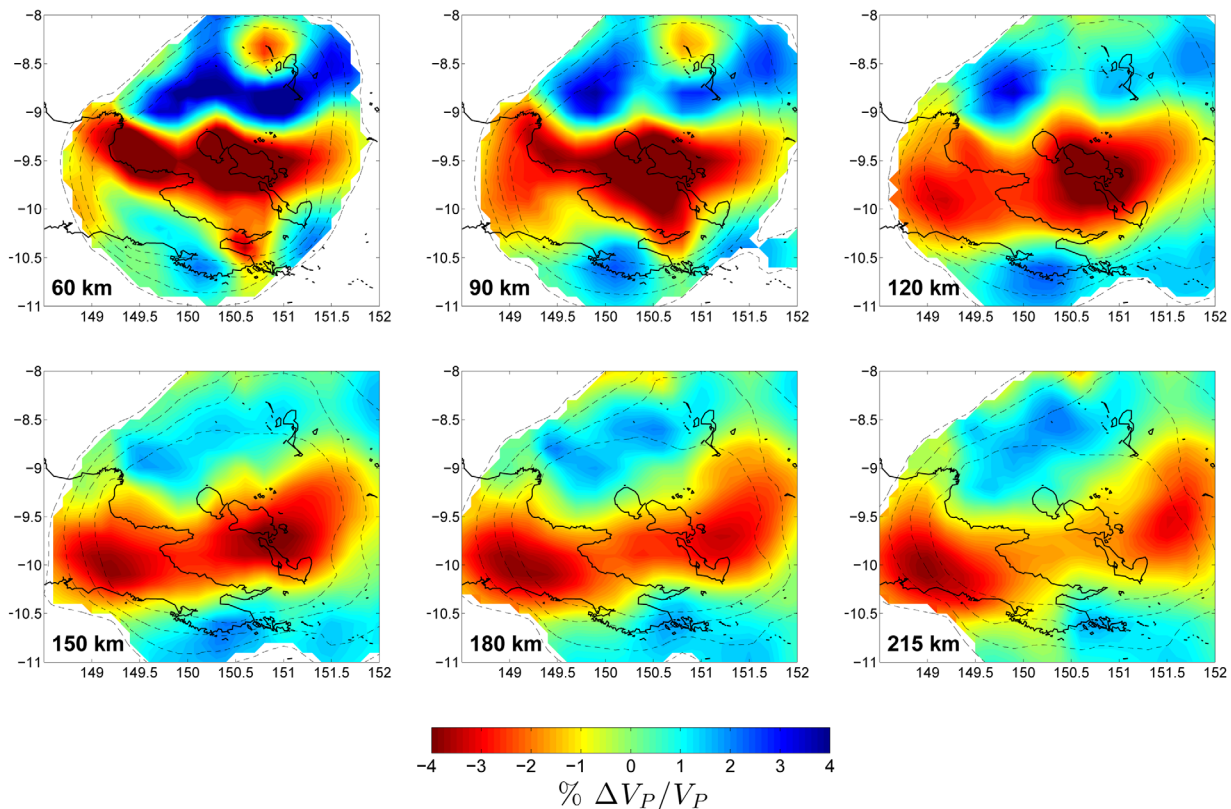
Figure 6. Variation in *P*-wave velocity plotted at different depths in the model domain, contoured for hit quality between 60 and 90%. Regions with hit quality < 60% are masked out.

on this model to interpret the structure and dynamics of this rift. The V_S model complements the V_P results and gives additional constraints on physical mechanisms of velocity heterogeneities.

Final station terms (computed by adding the prior crustal correction to the station statics from the inversion) strongly correlate with mean differential travel times at each station (Figure 3 and supporting information Table S1). These results agree with published moho maps showing shallow crust beneath the DEI grading to thicker crust on the rift shoulders [*Abers et al.*, 2002; *Obrebski et al.*, 2014]. Exceptions include stations on the Papuan Peninsula south of −10°S, which may not have thick crust, and station KIR on the Trobriand Islands where shallow fast velocity structure must be present.

4.1.1. V_P Model

The V_P model (Figures 6 and 8) shows an E-W swath of low velocities in the upper mantle beneath the DEI and extending westward toward the Papuan Peninsula, beneath Cape Vogel. The E-W slow structure has clear north and south limits and the $\delta V_P < -1\%$ region remains narrower than 100 km down to $\geq$180 km depth, beyond which synthetic tests indicate loss of resolution. These images are consistent with a previous *P*-wave tomography study centered to the east of our array [*Abers et al.*, 2002] and with surface waves (Jin et al., submitted manuscript, 2015).

The steep southward dip of the slow material in the western part of the model (Figure 8, section A-A′) may be present but is not a well constrained feature. Synthetic tests indicate that the apparent east-west bifurcation of the slow structure deeper than 200 km is an artifact resulting from diverging ray paths below the depth of good resolution. However, two interesting features that do appear to be robust are the broadening of the slow structure and the increase in amplitude of the slow anomaly going from west to east, in the direction of increasing extension (Figure 8, B-B′ and C-C′).

To the north of this slow rift there is a marked (2–3%) positive V_P anomaly between 8.5° and 9.0°S. The lateral continuity of the fast structure is less apparent in V_P than V_S but it seems to extend along strike (E-W) in the uppermost ∼100 km. There is a clear fast velocity region to the NW of Goodenough Island at 120 km
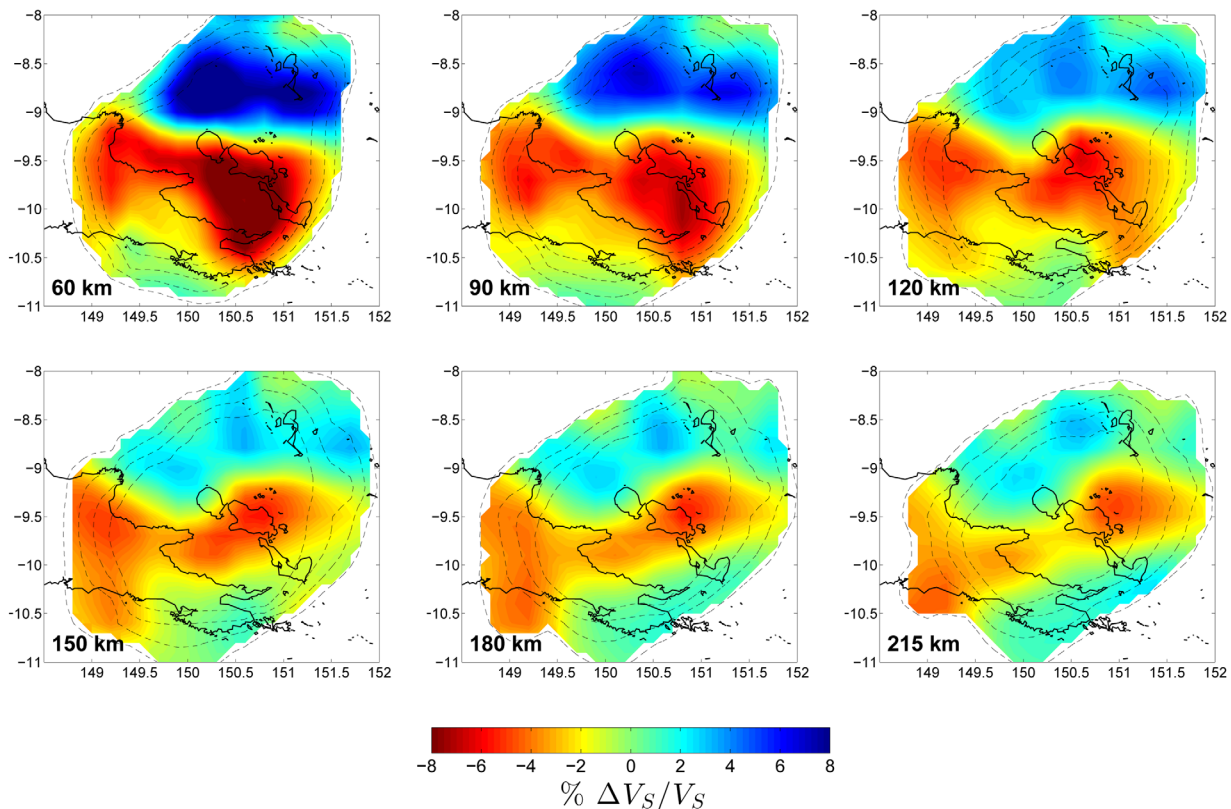
Figure 7. As for Figure 6 but for *S*-wave velocity.

depth that is in a region of the model that is well resolved. While this fast velocity structure is visible in the tomograms down to 180 km it becomes muted deeper than 135 km. Given the magnitude of this positive velocity anomaly, its well-defined boundaries, and the results of synthetic tests, the fast feature cannot be an side-lobe artifact of the tomography but represents faster-than-ambient mantle material. At a depth of 90 km there is a 6.5% peak-to-peak V_P variation; this magnitude of velocity heterogeneity is significantly greater than the typical value of <3% observed in other continental rifts [*Achauer and Masson*, 2002] and approaches values observed in back-arc settings [*Conder and Wiens*, 2006], or in the region of subducting plates [*Lay*, 1994]. The V_S model shows the same features, although slighly broader (Figure 7). Based on synthetic tests (section 3.4) and the fact that it is strongly dependent on the crustal model used, the discontinuous fast structure in the less-well resolved region south of the rift axis seems to be a side-lobe artifact.

4.1.2. V_S Model

The V_S model (Figure 7 and supporting information Figure S3) displays similar features to the V_P model in that there is a clear E-W trending low-velocity in the center of our model region and fast structure beneath the north of the array. In general, the V_S model shows less organized structure at depths greater than 120 km and squeezing tests demonstrate that no structure beneath 180 km is required by the data. The apparent southward step of the rift axis from east to west at $\geq$ 150 km depth is not well resolved.

In contrast to the V_P model, the low shear velocities appear to be much more concentrated at shallow depths beneath the DEI and, in particular, Goodenough Basin. Another distinction is that there is no clear southern boundary to the slow velocity structure along the rift axis. The fast structure beneath the Trobriand Platform is more laterally contiguous in V_S than in the V_P model, although squeezing tests indicate that it is not required to persist deeper than 120 km.

5. Local Seismicity

Earthquakes that occurred around the network were detected and located following procedures similar to *Li et al.* [2013], giving a catalog of 795 well-located hypocenters [*Dieck et al.*, 2013]. These earthquakes are
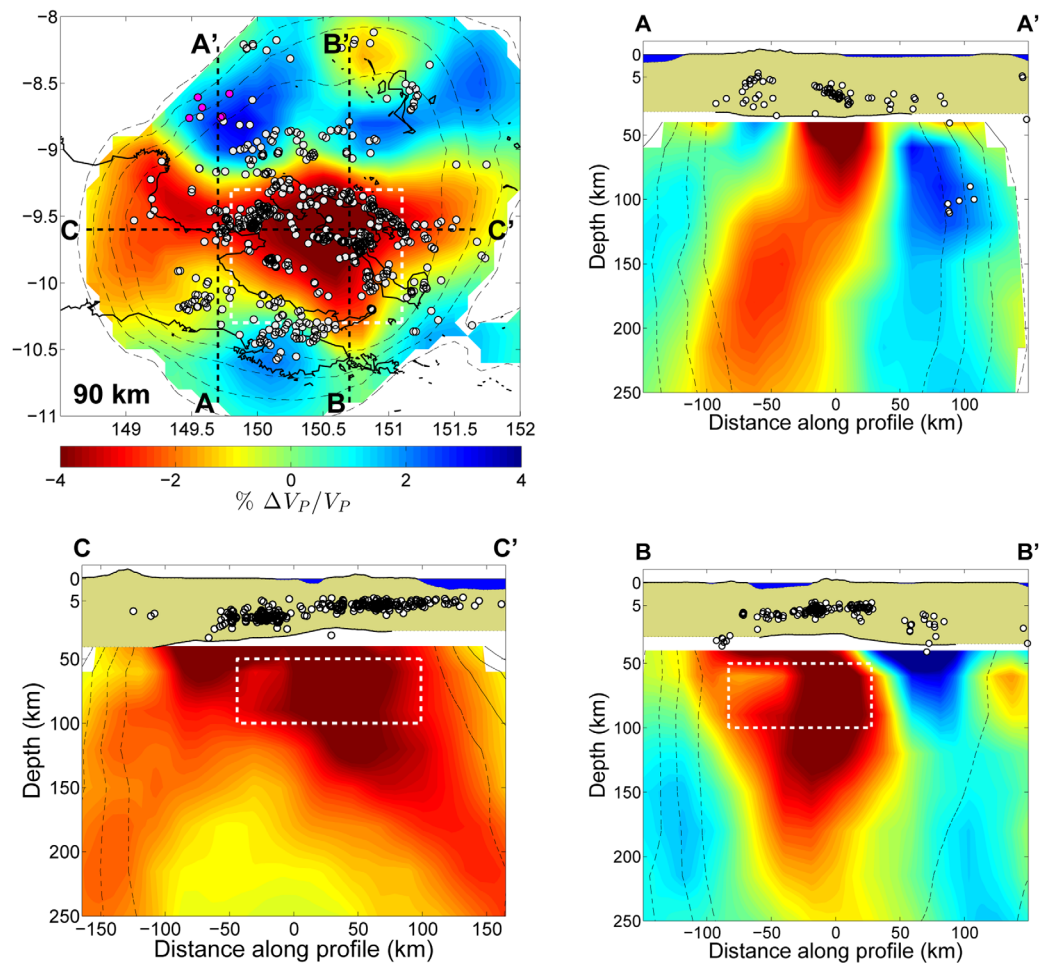
Figure 8. Three cross sections of *P*-wave velocity variation contoured for hit quality between 60 and 90%, where regions with hit quality < 60% are masked out. Locations of cross sections shown on 90 km horizontal slice. The moho plotted is to scale and derived from receiver functions. Note the change in vertical scale at 5 km: the topography is 3.5× exaggerated. Circles: seismicity from this study, relocated using HYPODD; plotted earthquakes have estimated 3-D location uncertainties <2.5 km and intermediate depth earthquakes are plotted in magenta. For the vertical slices only earthquakes within 25 km of the section are shown. White box is region with possible melt, indicated by triangles on Figure 10.

located in a one-dimensional velocity model determined from the 1999–2000 WOODSEIS seismic array overlapping with the eastern edge of the present study region [*Ferris et al.*, 2006], and have formal location errors less than 7 km vertically and 5 km horizontally. Improved locations were then obtained using the double-difference algorithm HYPODD [*Waldhauser and Ellsworth*, 2000]. Together with a previous seismicity study farther east [*Ferris et al.*, 2006] these earthquakes outline a belt of crustal deformation extending westward from the oceanic rift tip at 151.7°E (Figure 9).

Most earthquakes ring Goodenough and Fergusson Islands where faults bounding the metamorphic core complexes have been previously inferred [e.g., *Davies and Warren*, 1988; *Little et al.*, 2011]. Seismicity demonstrates that these faults are actively accommodating ongoing dome exhumation, both on the north and south sides of these domes, in agreement with GPS data [*Wallace et al.*, 2014]. The catalogue includes diffuse seismicity all along the Papuan Peninsula at crustal depths, including a southward step from the DEI to the Papuan mainland that indicates the Dayman-Suckling massif is the along-strike continuation of the chain of domes exhumed as part of the shallow extension process. Despite the good network coverage and geodetic evidence for motion here [*Wallace et al.*, 2014], few earthquakes are observed along the Goodenough Fault (Figure 2). These results will be discussed in more detail in a subsequent paper.

One of the most unexpected findings in the seismicity catalog is a group of six to eight well-located earthquakes at intermediate depths, 90–120 km, near (8.7°S, 149.7°E), with others farther west outside of the
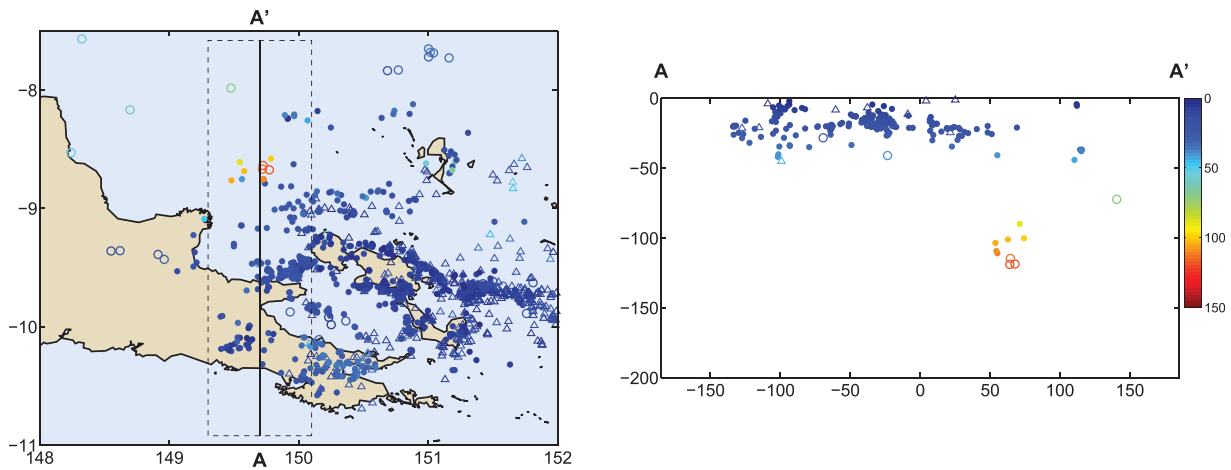
Figure 9. Plot of earthquakes in the region of our array. Earthquakes observed in this study (filled circles) or the Woodseis deployment (triangles) [*Ferris et al.*, 2006] were relocated using the HYPODD method; only events with estimated 3-D location uncertainties less than 2.5 km are plotted. Open circles: events from the EHB catalog [*Engdahl et al.*, 1998] for the period 1964–2002 (plotting only events constrained with at least one depth phase). The cross section shown has no vertical exaggeration.

network. These earthquakes occur at the same depths as those from which nearby UHP rocks were exhumed at 5–8 Ma and are the first well-located subcrustal earthquakes located within the Woodlark-D'Entrecasteaux Rift region, although intermediate-depth earthquakes have been documented 200 km farther west beneath the center of the Papuan Peninsula [e.g., *Abers and Roecker*, 1991; *Pegler et al.*, 1995]. Modern catalogs such as EHB [*Engdahl et al.*, 1998] show that the intermediate-depth earthquake zone extends from the Papuan Peninsula ESE and shallows to the region of the earthquakes we report here (Figure 9). These earthquakes almost directly underlie the western part of the array and are well-recorded by
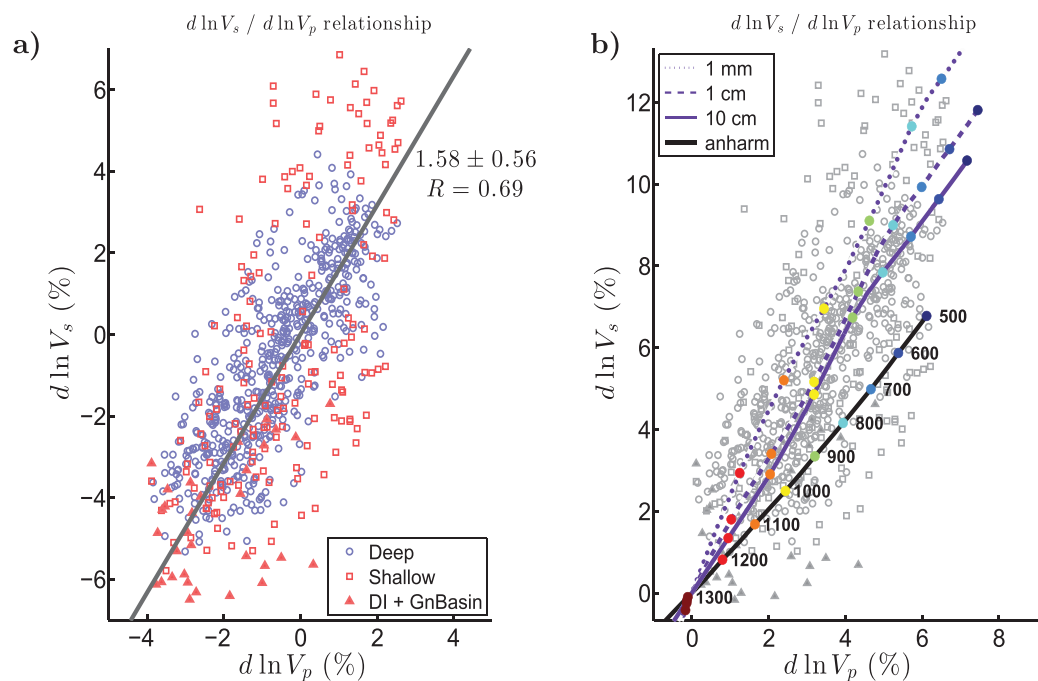

Figure 10. a) Plot of *S* versus *P* model velocity variations at common nodes, subdivided into the upper and lower parts of the model. Only nodes with hit quality > 0.7 are plotted, and the extreme 5% of velocity heterogeneities are ignored. Triangles (on both plots): shallow nodes beneath the D'Entrecasteaux Islands and Goodenough Basin (white boxes, Figure 10). The best-fit slope for all the nodes, constrained to [0,0], is found by orthogonal regression, minimizing weighted misfit to both δV_S and δV_P, giving: $m = 1.58 \pm 0.56$ (2σ bounds), with a correlation coefficient of 0.69. b) Predicted covariation of anelastic velocity variations with temperature at 95 km depth, assuming $T_{pot} = 1250°$C and dT/dz = 0.4 K/km. Different curves correspond to different grain sizes (see legend), as well as the anharmonic prediction. Full details in section 6.2.

the OBS's above them; all have at least one station within 40 km of the epicenter and are located by at least 10 phases, leading to formal errors in depth less than 1.5 km and horizontal errors less than 3.0 km. Thus, it is highly unlikely that these are mislocated in depth significantly.

6. Discussion

6.1. The Rift Axis

We have imaged the axis of the rift represented by an E-W structure of low seismic velocities in the upper mantle. This body is co-located with the shallowest Moho observed in receiver functions [*Abers et al.*, 2002; *Obrebski et al.*, 2014], the region of highest heat flow [*Martinez et al.*, 2001], and Quaternary surface volcanism [*Smith*, 1982]. The low velocities in the center of the rift lie directly along strike from the youngest spreading center at 151.5°E, and continue at least 250 km to 149°E. The amplitude of the δV_P anomaly suggests almost total lithospheric removal, implying mantle divergence and adiabatic upwelling of asthenosphere considerably ahead of the propagation of seafloor spreading (in agreement with spreading-related anisotropic fabric [*Eilon et al.*, 2014a] and some other continental rifts [e.g., *Rychert et al.*, 2012]).

The velocity models indicate that the rift remains relatively narrow: the $\delta V_P < -1\%$ region remains <100 km wide along strike and to the maximum depth it is resolved. Its width at 60 km depth increases from ∼60 to 100 km going from 149.5 to 151.0°E, in the direction of increasing extension. The crustal seismicity overlies the low velocities down to >150 km depth, demonstrating the localized and vertical nature of the rifting (Figure 8). Squeezing tests indicate that the velocity anomaly is not required by the data deeper than ∼180 km.

The narrow profile of the low-*V* region to depth is similar to that observed in the Main Ethiopian Rift (MER) [*Bastow et al.*, 2005; *Hammond et al.*, 2013] but more localized than Rio Grande [*Wilson et al.*, 2005; *Gao*, 2004] or Baikal [*Gao*, 2003] and contrasts with the wide triangular zone of upwelling thought to exist beneath mid-ocean ridges undergoing classic corner flow [*Hammond and Toomey*, 2003]. *Buck* [1991] demonstrated that narrow continental rifts are favored by cold geotherms, thin (<40 km) crust, and high strain rates - all features exhibited by this rift system. They also found that model core complexes form in areas of high geothermal gradient, raising interesting questions about their formation here where mean heat flow is low for a rift (∼70 mW m^{-2} [*Martinez et al.*, 2001]). Very low rift velocities at all depths can be reconciled with low heat flow in Goodenough Basin if they are localized to the immediate north of the basin, and/or if the mantle rifting is significantly younger than the crustal conductive heating timescale.

Strain localization may also arise as a result of prior viscosity heterogeneity; perhaps previous subduction has resulted in a weak corridor of mantle that could be exploited by incipient extension (e.g., in the hydrated mantle wedge and/or beneath the active arc [cf. *Dixon et al.*, 2004; *Kirby et al.*, 2014]). The rift may no longer be wet; our data do not require the large $\delta \ln V_S / \delta \ln V_P$ expected for water in nominally anhydrous minerals (section 6.2). Furthermore, the presence of basaltic volcanism along the rift axis probably requires temperatures too high to sustain water stored this way at depth [*Hirth and Kohlstedt*, 1996]. Despite this, *Ruprecht et al.* [2013] found >3 wt% H_2O primary melt content in Goodenough Island lavas—these are derived from the shallow region where we note large $\delta \ln V_S$ excursions (section 6.2).

Another local factor that might facilitate strain focussing is the presence of a cold, high-viscosity structure adjacent to the rift (section 6.3). In addition, high topography resulting from the Eocene Papuan orogen could have provided potential energy responsible for accelerating extension.

6.2. Physical Mechanisms for Velocity Heterogeneities

Plotting the relative perturbations in V_P and V_S for each node in our model yields arrays of points (Figure 10) with a slope $\delta \ln V_S / \delta \ln V_P$ that is diagnostic of physical mechanism, given assumptions regarding composition, pore structure, and anelastic effects. Steeper slopes indicate a stronger variation in shear modulus than bulk modulus, where $1.2 \leq \delta \ln V_S / \delta \ln V_P \leq 2.0$ is compatible with thermal heterogeneity alone [*Anderson et al.*, 1992] while $\delta \ln V_S / \delta \ln V_P > 2.0$ requires some mechanism (e.g., partial melt, water) to preferentially depress the shear modulus.

Our data (Figure 10) give a $\delta \ln V_S / \delta \ln V_P$ of 1.58 for the entire model volume, with an estimated 95% uncertainty of ± 0.56 and a correlation coefficient (R) of 0.69. Subdividing the model space above and below

100 km shows that the upper part of the model has more scatter ($R = 0.67$) than the part deeper than 100 km ($R = 0.79$) and a steeper slope (1.80 ± 0.99 versus 1.40 ± 0.45), although the difference is not statistically significant.

While slope analysis provides only a lower bound on $\delta \ln V_S / \delta \ln V_P$ (because V_S is more smoothed than V_P both intrinsically and by regularization), the observed slope matches predicted temperature-dependent velocity variations (Figure 10). Applying the scaling relationships of *Jackson and Faul* [2010] we compute $\delta \ln V_S$ and $\delta \ln V_P$ over a range of temperatures below $T_{adiabat}$ at 95 km depth for relevant grain sizes (between 1 mm and 100 mm [*Behn et al.*, 2009]), using the mean center frequencies of our measurements. We assume a mantle potential temperature of 1250°C based on DEI tephra [*Ruprecht et al.*, 2013] and use anharmonic $V(P, T)$ for pyrolite computed using HeFESTo [*Stixrude and Lithgow-Bertelloni*, 2011]. For 10 mm grains the predicted $\delta \ln V_S / \delta \ln V_P$ is 1.62, similar to the mean value (over a range of depths) from our model, supporting a predominantly thermal control on ΔV in this area.

We may not formally reject the hypothesis that the shallow part of the model is also recording only temperature heterogeneity but other factors may also be important. Strong anisotropy in this region [*Eilon et al.*, 2014a] may bias estimates of $\delta \ln V_S / \delta \ln V_P$ [*Hacker and Abers*, 2012] as might compositional heterogeneities associated with recent subduction (section 6.3). Moreover, several model nodes scatter toward large values of $|\delta \ln V_S / \delta \ln V_P|$. In particular, shallow nodes lying beneath the DEI and Goodenough Basin (Figure 8, white box; Figure 10, triangles) plot up to 4% below the main trend in $\delta \ln V_S / \delta \ln V_P$ suggesting the presence of melt or volatiles, in spatial agreement with the surface volcanism, and consistent with a surface wave study showing very low V_S immediately below the crust in the rift axis (Jin et al., submitted manuscript, 2015). Nonetheless, our results do not support the presence of large volumes of melt within the rift axis, in contrast to the MER [*Bastow et al.*, 2005; *Rychert et al.*, 2012]. The relative paucity of melt in this rift (despite likely hydration) may be due to the low mantle potential temperature [*Ruprecht et al.*, 2013] compared to, for example, the plume-influenced convecting mantle beneath the MER [*Bastow et al.*, 2008] or the western U.S. [*Wang et al.*, 2013].

6.3. Intermediate Depth Seismicity and Fast Structure

Intermediate depth seismicity in this region (section 5) is definitive evidence of cold, seismogenic material in the upper mantle; earthquakes in subducting slabs are thought to occur at temperatures less than 700–800°C [*Peacock*, 2001; *Hacker et al.*, 2003]. The hypocenters that fall within our array, and that have the smallest formal errors, are situated within the fast velocity structure in the northeast of the V_P model at the same depth, near 8.7°S, 149.8°E. We infer that temperatures in the high-velocity body do not exceed 700–800°C and that the positive δV_P structure is not only fast relative to the average model velocity at that depth but is cold and seismically fast in an absolute sense. Our calculations show that a $\sim$700°C structure adjacent to $\sim$1300°C adiabatically rifted mantle would produce the observed large ($\Delta V_P \sim 6.5\%$) velocity perturbations (Figure 10) irrespective of whether the fast mantle structure is depleted [*Schutt and Lesher*, 2006]. The independent observations of seismicity and ΔV provide an unusually specific constraint on steep lateral thermal gradients in a rifting context.

The southern boundary of the fast structure is well resolved and observable from back azimuthal variation in the differential travel times (Figure 3). The northern, western, and eastern limits of the fast region at the edge of our array are not well constrained. This body appears somewhat discontinuous in the V_P model but to have greater along-strike contiguity in the V_S model (which has stronger smoothing). Our models constrain only deviations from average layer velocity but, assuming the rift axis material is at similar velocity with depth (along a mantle adiabat), the diminished relative amplitude of the fast structure deeper than 130 km is persuasive evidence of its limited depth extent.

Interpretations for this structure include: a subducted slab, a cold nose associated with previous subduction, or a lithospheric instability (Figure 11). Unusually cold structure at depth likely extends over a large region. The >70 km deep earthquakes within our array lie within a band of diffuse intermediate depth seismicity extending $\sim$500 km WNW beneath the Papuan Peninsula, although dip and lateral contiguity of this band are unclear [*Abers and Roecker*, 1991]. Similarly, our tomographic images do not show a clear dip to the fast region, nor do the earthquakes in our study exhibit a Wadati-Benioff zone with discernible directionality. This young and tectonically active region is far from any cratonic continental interior and so the prerifting
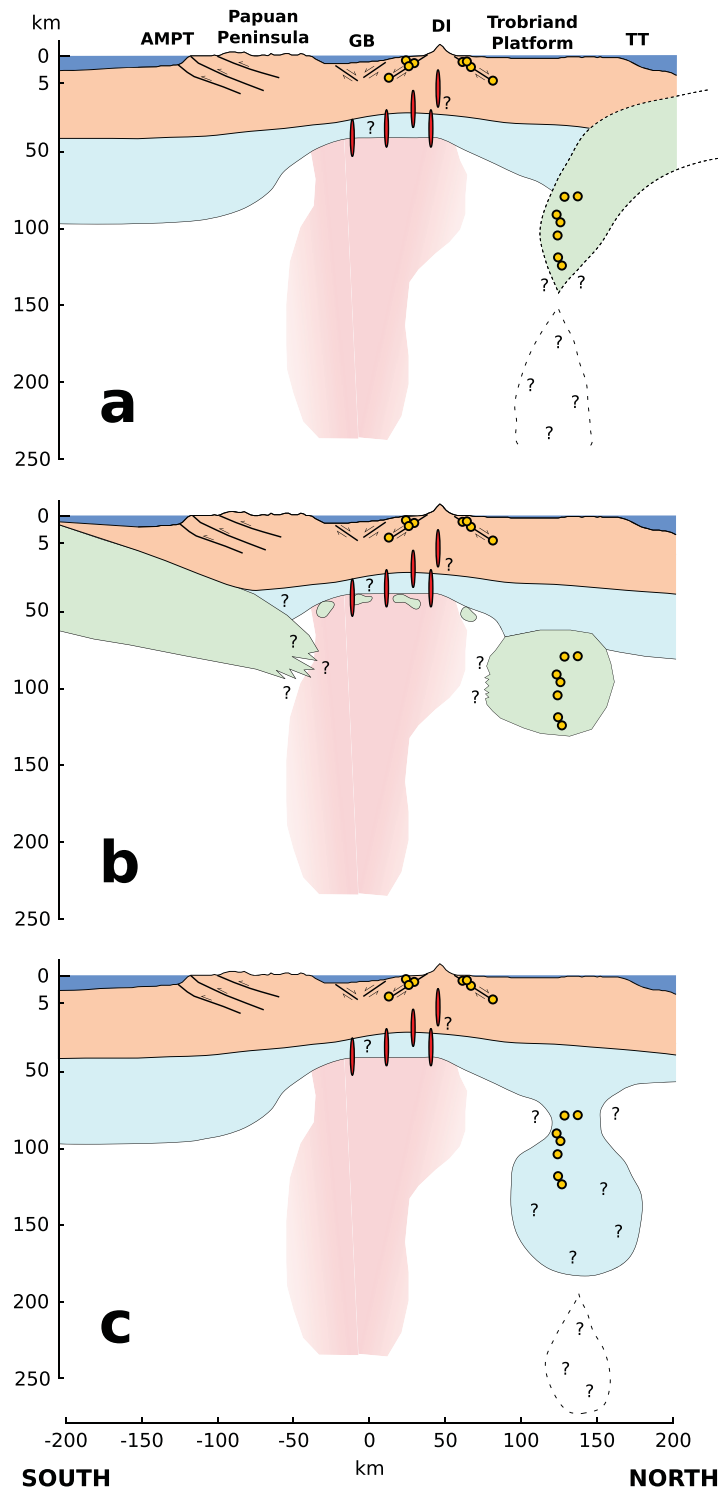
Figure 11. Cartoons of the rift showing different interpretations of the fast structure in the north of the models as representing (a) a slab fragment from southward subduction at the Trobriand Trough, (b) a slab fragment broken off by rifting of underthrust lithosphere from northward subduction at the Aure-Moresby-Pocklington Trough, or (c) a lithospheric instability either left over from the Papuan Orogen or associated with rifting. Note 3.5× vertical exaggeration shallower than 5 km. GB: Goodenough Basin, other abbreviations in text.

lithospheric thickness is not thought to have been large but to have formed in Cenozoic accretionary events.

6.3.1. A Relic of Subduction

The fast structure may represent a hitherto unrecognized subducted slab or cold nose of a mantle wedge related to subduction at either the Trobriand Trough (TT) or Aure-Moresby-Pocklington Trough (AMPT). Both candidate subduction boundaries are roughly parallel to the scattered trend of intermediate depth seismicity beneath the Papuan Peninsula and (in the southeast) a roughly E-W trend of Holocene volcanism through the DEI that bears hallmarks of a subduction-enriched source [*Smith and Milsom*, 1984]. With no resolvable dip the earthquakes corroborate neither scenario [*Abers and Roecker*, 1991]. The main faults on the Papuan Peninsula are all north dipping [*Davies*, 2012; *Daczko et al.*, 2009] but these largely reflect the Eocene orogeny and do not preclude subsequent south-vergent thrusting. Regional studies have not found tomographic evidence for subduction in the vicinity [*Hall and Spakman*, 2002] although their resolution in the uppermost mantle is likely to be poor away from seismically active slabs.

Several authors [*Pegler et al.*, 1995; *Yan and Kroenke*, 1993; *Cooper and Taylor*, 1987; *Davies et al.*, 1987; *Fitz and Mann*, 2013] have postulated southward subduction of the oceanic Solomon Sea at the TT, which may have terminated with the onset of northward subduction at New Britain and the San Cristobal trenches [*Yan and Kroenke*, 1993] leaving a dangling slab (Figure 11a) at shallow depth. At present the TT is largely aseismic, with just a single (normal faulting) $M_W > 6$ earthquake instrumentally

recorded, and plate motion estimates are difficult to reconcile with any convergence at this boundary [*Wallace et al.*, 2014, 2004]. Thus, evidence for ongoing subduction at this boundary is weak, although the trough may have been the site of significant convergence at some time in the past.

Alternatively, Cenozoic convergence at the AMPT has been linked to northward subduction of the leading edge of the Australian margin. Subducted material could have been rafted ∼200 km northward by recent extension to now lie north of the rift (Figure 11b). This scenario is attractive because it involves the subduction of continental material into the source region of the continentally derived UHP rocks found within the DEI. The timing and dynamics of UHP exhumation would then be dictated by breakup of underthrust Australian lithosphere during rifting; incomplete breakup or underplating of this felsic material where less extension has occurred could explain low sub-Moho velocities west of Goodenough Island (Jin et al., submitted manuscript, 2015). However, Eocene AMPT subduction [*Yan and Kroenke*, 1993] may be incompatible with observed seismogenicity and low temperatures because a 100 km thick lithospheric slab heated from both sides would warm with an e-folding timescale of ∼32 Myr. *Webb et al.* [2014] and *Mutter* [1975] suggest AMPT subduction in the mid-Miocene (∼12–13 Ma) but symmetric magnetic anomalies in the Coral Sea to the south permit only limited AMPT subduction since 56 Ma [*Weissel and Watts*, 1979].

6.3.2. Lithospheric Instability?
Our observations provide an unusually well imaged juxtaposition of hot rift axis and cold dangling lithosphere, whatever its origin where the combination of velocity information and seismicity delineates a sharp lateral gradient of ∼700 K over <70 km. Such large thermal (and, hence, density) contrast implies the system may be gravitationally unstable.

Mareschal [1983] proposed that rapid zones of extension such as this one require lithospheric delamination, a process which has been implicated in the development of metamorphic core complexes [*Molnar*, 2015; *Lachenbruch et al.*, 1994] and which could contribute to rapid UHP exhumation during rifting [*Little et al.*, 2011; *Ellis et al.*, 2011]. *Abers and Roecker* [1991] postulated that the intermediate depth seismicity beneath the Papuan Peninsula north of ∼8.5° S could be explained by lithospheric convective instability (drip) just as well as any proposed subduction, suggesting that volcanism on the DEI represents a region where a continental lithospheric root has already detached (Figure 11c); this interpretation is similar to that suggested for intermediate depth earthquakes and fast mantle structures in the Carpathians [*Ren et al.*, 2012]. However, assuming mantle lithosphere viscosity of 10^{23} Pa s [*Burov*, 2009] convective instabilities would grow with a characteristic time scale of 500–800 Myr, about 10–100× longer than available here, permitting long-lived slab fragments [*Wang et al.*, 2013]. Stratigraphy provides an important constraint on this process: sediments younger than 8.4 Ma on the Trobriand Platform do not permit more than ∼500 m of recent vertical displacement [*Fitz and Mann*, 2013], precluding significant dynamic or isostatic topography associated with the fast structure and indicating slow or negligible instability growth.

Still, some mechanism must exist to remove the lithosphere beneath the rift axis prior to the onset of seafloor spreading. Small scale convection associated with the horizontal temperature gradient could facilitate rifting [*Buck*, 1986] and result in large velocity contrasts [*Hieronymus et al.*, 2007] as seen in our imaging. It is possible that the introduction of water by prior subduction could hasten convective processes by lowering mantle viscosity and facilitating lithospheric removal.

If lithospheric instability or small scale convection have not influenced rifting it is not clear how the hot shallow temperature at the rift axis has been achieved so rapidly. The discrepancy between apparently limited crustal thinning and lithospheric removal in this rift is not consistent with pure shear extension models [*Mckenzie*, 1978] and perhaps necessitates lower crustal flow, a process which has been frequently linked to development of metamorphic core complexes [*Buck*, 1988].

6.4. Relationship to UHP Rocks
The inferred temperatures within the fast structure of ≤700°C at ∼100 km depth are very similar to the maximum pressure and temperature recorded by the UHP rocks. The intermediate-depth seismicity lies along strike to the east, and somewhat north, of the metamorphic core complexes. Speculatively, the UHP rocks could have formed in a continuation or extension of the same cold body at depth, prior to extension. Parts of this body closest to the rift axis could have been entrained in exhumation processes related to the rifting, while other fragments of the same body were not. Alternatively, no direct connection exists between

this slab fragment and the UHP rocks at the surface; the P, T coincidence reflects the Earth's common subduction geotherms rather than a causal link. That said, the presence of this deep, cold material close to the along-strike continuation of the present metamorphic core complexes (not including the Suckling-Dayman massif) is circumstantial evidence that the fast structure in our models is related to the UHP source. Petersen and Buck (submitted manuscript, 2015) model rapid UHP exhumation in the Woodlark Rift by extension and eduction (reversal of subduction) of continental material on a north dipping subduction plane. If the high-V_P structure we image is a slab fragment, their geodynamical model may explain the cessation of subduction and exhumation of material from UHP depths within a rift that has asymmetry similar to our tomographic cross sections, although with opposite polarity.

7. Conclusions

We have conducted a detailed seismic investigation of the Woodlark Rift beneath the DEI, imaging the rifted continent. A narrow low-velocity structure extends along strike from the nearby spreading centers >250km into the extended continent; this structure correlates with surficial volcanism and the thinnest crust seen in receiver functions and indicates marked thinning of lithosphere along the rift axis far ahead of sea floor spreading.

The continental rift remains narrow to depth. We posit that high volatile content in a relict mantle wedge, as well as the contrast in strength between asthenosphere and a dangling slab, facilitated strain localization processes that are expected in rapidly extending rifts such as this one.

Well-located intermediate depth earthquakes in this region are co-located with a fast velocity structure in our V_P and V_S tomographic models. Several alternatives exist that would allow the subduction of cold material to these depths at some time prior to the onset of rifting; the models do not clearly define a dip to the fast region. The juxtaposition of this cold, fast lithosphere with hot, slow rifted mantle explains the large peak-to-peak velocity contrast in our images. The longevity of this feature is an open question, given the gravitational instability implied by the strong thermal contrast between dangling lithosphere and upwelling asthenosphere.

Both seismicity and velocity heterogeneities indicate that the fast structure in our models is at similar P,T conditions to those recorded by the coesite-eclogite sample, along strike from the present-day core complexes. This may represent un-exhumed material awaiting sufficient overlying crustal extension before beginning ascent, or simply a remnant of the subduction system that advected the UHP rocks' protoliths to depth.

References

Abers, G. A., and S. W. Roecker (1991), Deep structure of an arc-continent collision: Earthquake relocation and inversion for upper mantle P and S wave velocities beneath Papua New Guinea, *J. Geophys. Res.*, *96*, 6379–6401.

Abers, G. A., C. Z. Mutter and J. Fang (1997), Shallow dips of normal faults during rapid extension: Earthquakes in the Woodlark-D'Entrecasteaux rift system, Papua New Guinea, *J. Geophys. Res.*, *102*, 15–15.

Abers, G. A., A. Ferris, M. Craig, H. L. Davies, A. L. Lerner-Lam, J. C. Mutter, and B. Taylor (2002), Mantle compensation of active metamorphic core complexes at Woodlark rift in Papua New Guinea, *Nature*, *418*, 862–865.

Achauer, U., and F. Masson (2002), Seismic tomography of continental rifts revisited: From relative to absolute heterogeneities, *Tectonophysics*, *358*(1-4), 17–37.

Aki, K., A. Christoffersson, and E. S. Husebye (1977), Determination of the three-dimensional seismic structure of the lithosphere, *J. Geophys. Res.*, *82*, 277–296.

Anderson, O. L., D. Isaak, and H. Oda (1992), High-temperature elastic constant data on minerals relevant to geophysics, *Rev. Geophys.*, *30*, 57–90.

Baldwin, S. L., B. D. Monteleone, L. E. Webb, P. G. Fitzgerald, M. Grove, and E. J. Hill (2004), Pliocene eclogite exhumation at plate tectonic rates in eastern Papua New Guinea, *Nature*, *431*, 263–267.

Baldwin, S. L., L. E. Webb, and B. D. Monteleone (2008), Late Miocene coesite-eclogite exhumed in the Woodlark Rift, *Geology*, *36*(9), 735–738.

Bastow, I. D., G. W. Stuart, J. M. Kendall, and C. J. Ebinger (2005), Upper-mantle seismic structure in a region of incipient continental breakup: Northern Ethiopian rift, *Geophys. J. Int.*, *162*(2), 479–493.

Bastow, I. D., A. A. Nyblade, G. W. Stuart, T. O. Rooney, and M. H. Benoit (2008), Upper mantle seismic structure beneath the Ethiopian hot spot: Rifting at the edge of the African low-velocity anomaly, *Geochem. Geophys. Geosyst.*, *9*, Q12022, doi:10.1029/2008GC002107.

Behn, M. D., G. Hirth, and J. R. Elsenbeck II (2009), Implications of grain size evolution on the seismic structure of the oceanic upper mantle, *Earth Planet. Sci. Lett.*, *282*(1-4), 178–189.

Bijwaard, H., and W. Spakman (2000), Non-linear global P-wave tomography by iterated linearized inversion, *Geophys. J. Int.*, *141*, 71–82.

Buck, W. R. (1986), Small-scale convection induced by passive rifting: The cause for uplift of rift shoulders, *Earth Planet. Sci. Lett.*, *77*(3-4), 362–372.

Buck, W. R. (1988), Flexural rotation of normal faults, *Tectonics*, *7*, 959–973.

Buck, W. R. (1991), Modes of continental lithospheric extension, *J. Geophys. Res.*, *96*, 161–120.

Burov, E. B. (2009), Plate rheology and mechanics, in *Crust and Lithosphere Dynamics*, *Treatise on Geophysics*, vol. 6, edited by A. B. Watts, chap. 3, pp. 99–151, Elsevier. [Available at http://www.sciencedirect.com/science/article/pii/B9780444527486001024.]

Conder, J. A., and D. A. Wiens (2006), Seismic structure beneath the Tonga arc and Lau back-arc basin determined from joint Vp, Vp/Vs tomography, *Geochem. Geophys. Geosyst.*, *7*, Q03018, doi:10.1029/2005GC001113.

Cooper, P., and B. Taylor (1987), Seismotectonics of New Guinea: A model for arc reversal following arc-continent collision, *Tectonics*, *6*, 53–67.

Crotwell, H. P., T. J. Owens, and J. Ritsema (1999), The TauP toolkit: Flexible seismic travel-time and ray-path utilities, *Seismol. Res. Lett.*, *70*(2), 154–160.

Daczko, N. R., P. Caffi, J. A. Halpin, and P. Mann (2009), Exhumation of the Dayman dome metamorphic core complex, eastern Papua New Guinea, *J. Metamorphic Geol.*, *27*, 405–422.

Dahlen, F. A., S. H. Hung, and G. Nolet (2000), Fréchet kernels for finite-frequency traveltimes—I. Theory, *Geophys. J. Int.*, *141*(1), 157–174.

Davies, H. L. (2012), The geology of New Guinea - The cordilleran margin of the Australian continent, *Episodes*, *35*(1), 87–102.

Davies, H. L., and A. L. Jaques (1984), Emplacement of ophiolite in Papua New Guinea, *Geol. Soc. Spec. Publ.*, *13*(1), 341–349.

Davies, H. L., and R. G. Warren (1988), Origin of eclogite-bearing, domed, layered metamorphic complexes ("core complexes") in the D'Entrecasteaux islands, Papua New Guinea, *Tectonics*, *7*, 1–21.

Davies, H. L., E. Honza, D. L. Tiffin, J. Lock, Y. Okuda, J. B. Keene, F. Murakami, and K. Kisimoto (1987), Regional setting and structure of the western Solomon Sea, *Geo Mar. Lett.*, *7*(3), 153–160.

Dieck, C. C., G. A. Abers, Z. Eilon, J. B. Gaherty, and R. Verave (2013), Seismicity in an active rift exposing ultra-high pressure metamorphic rocks: D'Entrecasteaux Islands, Papua New Guinea, Abstract #T21A–2524 presented at 2013 Fall Meeting, AGU, San Francisco, Calif.

Dixon, J. E., T. H. Dixon, D. R. Bell, and R. Malservisi (2004), Lateral variation in upper mantle viscosity: Role of water, *Earth Planet. Sci. Lett.*, *222*(2), 451–467.

Eilon, Z., G. A. Abers, G. Jin, and J. B. Gaherty (2014a), Anisotropy beneath a highly extended continental rift, *Geochem. Geophys. Geosyst.*, *15*, doi:10.1002/2013GC005092.

Eilon, Z., G. A. Abers, J. B. Gaherty, and G. Jin (2014b), A joint inversion for velocity and anisotropy structure beneath a highly extended continental rift, Abstract #T54A-06 presented at 2014 Fall Meeting, AGU, San Francisco, Calif.

Ellis, S. M., T. A. Little, L. M. Wallace, B. R. Hacker, and S. J. H. Buiter (2011), Feedback between rifting and diapirism can exhume ultrahigh-pressure rocks, *Earth Planet. Sci. Lett.*, *311*, 427–438.

Engdahl, E. R., R. van der Hilst, and R. P. Buland (1998), Global teleseismic earthquake relocation with improved travel times and procedures for depth determination, *Bull. Seismol. Soc. Am.*, *88*(3), 722–743.

Ferris, A., G. A. Abers, B. Zelt, B. Taylor and S. W. Roecker (2006), Crustal structure across the transition from rifting to spreading: The Woodlark rift system of Papua New Guinea, *Geophys. J. Int.*, *166*(2), 622–634.

Fitz, G., and P. Mann (2013), Tectonic uplift mechanism of the Goodenough and Fergusson Island gneiss domes, eastern Papua New Guinea: Constraints from seismic reflection and well data, *Geochem. Geophys. Geosyst.*, *14*, 3969–3995, doi:10.1002/ggge.20208.

Gao, S. S. (2003), Evidence for small-scale mantle convection in the upper mantle beneath the Baikal rift zone, *J. Geophys. Res.*, *108*(B4), 2194, doi:10.1029/2002JB002039.

Gao, W. (2004), Upper mantle convection beneath the central Rio Grande rift imaged by P and S wave tomography, *J. Geophys. Res.*, *109*, B03305, doi:10.1029/2003JB002743.

Gordon, S. M., T. A. Little, B. R. Hacker, and S. A. Bowring (2012), Multi-stage exhumation of young UHP–HP rocks: Timescales of melt crystallization in the D'Entrecasteaux Islands, southeastern Papua New Guinea, *Earth Planet. Sci. Lett.*, *351–352*, 237–246.

Hacker, B. R., and G. A. Abers (2012), Subduction Factory 5: Unusually low Poisson's ratios in subduction zones from elastic anisotropy of peridotite, *J. Geophys. Res.*, *117*, B06308, doi:10.1029/2012JB009187.

Hacker, B. R., S. M. Peacock, and G. A. Abers (2003), Subduction factory 2. Are intermediate-depth earthquakes in subducting slabs linked to metamorphic dehydration reactions?, *J. Geophys. Res.*, *108*(B1), 2030, doi:10.1029/2001JB001129.

Hall, R., and W. Spakman (2002), Subducted slabs beneath the eastern Indonesia–Tonga region: Insights from tomography, *Earth Planet. Sci. Lett.*, *201*(2), 321–336.

Hammond, J. O. S., et al. (2013), Mantle upwelling and initiation of rift segmentation beneath the Afar Depression, *Geology*, *41*(6), 635–638.

Hammond, W. C., and D. R. Toomey (2003), Seismic velocity anisotropy and heterogeneity beneath the Mantle Electromagnetic and Tomography Experiment (MELT) region of the East Pacific Rise from analysis of *P* and *S* body waves, *J. Geophys. Res.*, *108*(B4), 2176, doi:10.1029/2002JB001789.

Hieronymus, C. F., Z. H. Shomali, and L. B. Pedersen (2007), A dynamical model for generating sharp seismic velocity contrasts underneath continents: Application to the Sorgenfrei–Tornquist Zone, *Earth Planet. Sci. Lett.*, *262*, 77–91.

Hirth, G., and D. L. Kohlstedt (1996), Water in the oceanic upper mantle: Implications for rheology, melt extraction and the evolution of the lithosphere, *Earth Planet. Sci. Lett.*, *144*(1-2), 93–108.

Jackson, I., and U. H. Faul (2010), Grainsize-sensitive viscoelastic relaxation in olivine: Towards a robust laboratory-based model for seismological application, *Phys. Earth Planet. Inter.*, *183*, 151–163.

Kennett, B. L. N., E. R. Engdahl, and R. P. Buland (1995), Constraints on seismic velocities in the Earth from traveltimes, *Geophys. J. Int.*, *122*(1), 108–124.

Kington, J. D., and A. M. Goodliffe (2008), Plate motions and continental extension at the rifting to spreading transition in Woodlark Basin, Papua New Guinea: Can oceanic plate kinematics be extended into continental rifts?, *Tectonophysics*, *458*(1-4), 82–95.

Kirby, S. H., K. Wang, and T. M. Brocher (2014), A large mantle water source for the northern San Andreas fault system: A ghost of subduction past, *Earth Planets Space*, *66*(1), 67–18.

Lachenbruch, A. H., J. H. Sass, and P. Morgan (1994), Thermal regime of the southern Basin and Range Province: 2. Implications of heat flow for regional extension and metamorphic core complexes, *J. Geophys. Res.*, *99*, 22,121–22,133.

Lay, T. (1994), Seismological constraints on the velocity structure and fate of subducting lithospheric slabs: 25 years of progress, *Adv. Geophys.*, *35*, 187.

Lévêque, J.-J., and F. Masson (1999), From ACH tomographic models to absolute velocity models, *Geophys. J. Int.*, *137*(3), 621–629.

Li, J., G. A. Abers, Y. Kim, and D. Christensen (2013), Alaska megathrust 1: Seismicity 43 years after the great 1964 Alaska megathrust earthquake, *J. Geophys. Res. Solid Earth*, *118*, 4861–4871, doi:10.1002/jgrb.50358.

Little, T. A., B. R. Hacker, S. M. Gordon, and S. L. Baldwin (2011), Diapiric exhumation of Earth's youngest (UHP) eclogites in the gneiss domes of the D'Entrecasteaux Islands, Papua New Guinea, *Tectonophysics*, *510*, 39–68.

Mareschal, J.-C. (1983), Mechanisms of uplift preceding rifting, *Tectonophysics*, *94*(1-4), 51–66.

Martinez, F., A. M. Goodliffe, and B. Taylor (2001), Metamorphic core complex formation by density inversion and lower-crust extrusion, *Nature*, *411*, 930–934.

Mckenzie, D. (1978), Some remarks on the development of sedimentary basins, *Earth Planet. Sci. Lett.*, *40*(1), 25–32.

Menke, W. (1984), *Geophysical Data Analysis: Discrete Inverse Theory*, 1st ed., Academic Press Inc., N. Y.

Menke, W., and Z. Eilon (2015), Relationship Between Data Smoothing and the Regularization of Inverse Problems, *Pure Appl. Geophys.*, pp. 1–16, doi:10.1007/s00024-015-1059-0.

Molnar, P. (2015), Gravitational instability of mantle lithosphere and core complexes, *Tectonics*, *34*, 478–487, doi:10.1002/2014TC003808.

Mutter, J. C. (1975), A structural analysis of the Gulf of Papua and Northwest Coral Sea Region, *Rep. 179*, 52 pp., Aust. Bur. of Miner. Resour. Geol. and Geophys.

Obrebski, M., G. A. Abers, G. Jin, and Z. Eilon (2014), Rift Structure in Eastern Papua New Guinea from the joint inversion of receiver functions and seismic noise, Abstract #T54A-07 presented at 2014 Fall Meeting 2014, AGU, San Francisco, Calif.

Paige, C. C., and M. A. Saunders (1982), LSQR: An algorithm for sparse linear equations and sparse least squares, *ACM Trans. Math. Software*, *8*(1), 43–71.

Peacock, S. M. (2001), Are the lower planes of double seismic zones caused by serpentine dehydration in subducting oceanic mantle?, *Geology*, *29*(4), 299–302.

Pegler, G., S. Das, and J. H. Woodhouse (1995), A seismological study of the eastern New Guinea and the western Solomon Sea regions and its tectonic implications, *Geophys. J. Int.*, *122*(3), 961–981.

Petersen, K. D., and W. R. Buck (2015), Eduction, extension, and exhumation of ultrahigh-pressure rocks in metamorphic core complexes due to subduction initiation, *Geochem. Geophys. Geosys.*, doi:10.1002/2015GC005847.

Ren, Y., G. W. Stuart, G. A. Houseman, and B. Dando (2012), Upper mantle structures beneath the Carpathian?Pannonian region: Implications for the geodynamics of continental collision, *Earth Planet. Sci. Lett.*, *349–350*, 139–152, doi:10.1016/j.epsl.2012.06.037.

Ruprecht, P., T. A. Plank, G. Jin, and G. A. Abers (2013), Rifting and UHP exhumation in Eastern Papua New Guinea: Temperature and pressure constraints from primitive magmas, Abstract #T21B-2559 presented at 2013 Fall Meeting, AGU, San Francisco, Calif.

Rychert, C. A., J. O. S. Hammond, and N. Harmon (2012), Volcanism in the Afar Rift sustained by decompression melting with minimal plume influence, *Nature*, *5*, 406–409.

Saltzer, R. L., and E. D. Humphreys (1997), Upper mantle P wave velocity structure of the eastern Snake River Plain and its relationship to geodynamic models of the region, *J. Geophys. Res.*, *102*(B6), 11829–11841.

Schmandt, B., and E. Humphreys (2010a), Seismic heterogeneity and small-scale convection in the southern California upper mantle, *Geochem. Geophys. Geosyst.*, *11*, Q05004, doi:10.1029/2010GC003042.

Schmandt, B., and E. Humphreys (2010b), Complex Subduction and small-scale convection revealed by body-wave tomography of the western United States upper mantle, *Earth Planet. Sci. Lett.*, *297*, 435–445.

Schutt, D. L., and C. E. Lesher (2006), Effects of melt depletion on the density and seismic velocity of garnet and spinel lherzolite, *J. Geophys. Res.*, *111*, B05401, doi:10.1029/2003JB002950.

Smith, I. E. (1982), Volcanic evolution in eastern Papua, *Tectonophysics*, *87*(1), 315–333.

Smith, I. E., and J. S. Milsom (1984), Late Cenozoic volcanism and extension in Eastern Papua, *Geol. Soc. Spec. Publ.*, *16*(1), 163–171.

Stixrude, L., and C. Lithgow-Bertelloni (2011), Thermodynamics of mantle minerals—II. Phase equilibria, *Geophys. J. Int.*, *184*(3), 1180–1213.

Taylor, B., A. M. Goodliffe, and F. Martinez (1999), How continents break up: Insights from Papua New Guinea, *J. Geophys. Res.*, *104*, 7497–7512.

VanDecar, J. C., and R. S. Crosson (1990), Determination of teleseismic relative phase arrival times using multi-channel cross-correlation and least squares, *Bull. Seismol. Soc. Am.*, *80*(1), 150–169.

Waldhauser, F. and W. L. Ellsworth (2000), A double-difference earthquake location algorithm: Method and application to the northern Hayward fault, California, *Bull. Seismol. Soc. Am.*, *90*(6), 1353–1368.

Wallace, L. M., C. Stevens, E. Silver, R. McCaffrey, W. Loratung, S. Hasiata, R. Stanaway, R. Curley, R. Rosa, and J. Taugaloidi (2004), GPS and seismological constraints on active tectonics and arc-continent collision in Papua New Guinea: Implications for mechanics of microplate rotations in a plate boundary zone, *J. Geophys. Res.*, *109*, B05404, doi:10.1029/2003JB002481.

Wallace, L. M., S. M. Ellis, T. Little, P. Tregoning, N. Palmer, R. Rosa, R. Stanaway, J. Oa, E. Nidkombu, and J. Kwazi (2014), Continental breakup and UHP rock exhumation in action: GPS results from the Woodlark Rift, Papua New Guinea, *Geochem. Geophys. Geosyst.*, *15*, 4267–4290, doi:10.1002/2014GC005458.

Wang, Y., D. W. Forsyth, C. J. Rau, N. Carriero, B. Schmandt, J. B. Gaherty, and B. Savage (2013), Fossil slabs attached to unsubducted fragments of the Farallon plate, *Proc. Natl. Acad. Sci. U. S. A.*, *110*(14), 5342–5346.

Webb, L. E., S. L. Baldwin, T. A. Little, and P. G. Fitzgerald (2008), Can microplate rotation drive subduction inversion?, *Geology*, *36*(10), 823–826.

Webb, L. E., S. L. Baldwin, and P. G. Fitzgerald (2014), The Early-Middle Miocene subduction complex of the Louisiade Archipelago, southern margin of the Woodlark Rift, *Geochem. Geophys. Geosyst.*, *15*, 4024–4046, doi:10.1002/2014GC005500.

Weissel, J. K., and A. B. Watts (1979), Tectonic evolution of the Coral Sea Basin, *J. Geophys. Res.*, *84*, 4572–4582.

Wilson, D., R. Aster, J. Ni, S. Grand, W. Gao, W. S. Baldridge, S. Semken, and P. Patel (2005), Lithospheric structure of the Rio Grande rift, *Nature*, *433*, 851–855.

Yan, C. Y., and L. W. Kroenke (1993), A plate tectonic reconstruction of the Southwest Pacific, 0–100 Ma, *Proc. Ocean Drill. Program Sci. Results,* 130, 697–709.

Zelt, C. A. (1998), Lateral velocity resolution from three-dimensional seismic refraction data, *Geophys. J. Int.*, *135*(3), 1101–1112.